









Laser-assisted rapid prototyping of silica optical fibers functionalized with nanodiamonds and multiple active rare earth dopants

PASCAL HÄNZI,¹  DARIUSZ PYSZ,² MARIUSZ MRÓZEK,³  ROBERT BOGDANOWICZ,⁴  RYSZARD BUCZYŃSKI,^{2,5}  MARIUSZ KLIMCZAK,⁵  THOMAS FEURER,¹ VALERIO ROMANO,¹ AND ALEXANDER M. HEIDT^{1,*} 

¹*Institute of Applied Physics, University of Bern, Sidlerstrasse 5, 3012 Bern, Switzerland*

²*Łukasiewicz Research Network, Institute of Microelectronics and Photonics, Al. Lotników 32/46, 02-668 Warsaw, Poland*

³*Institute of Physics, Jagiellonian University in Kraków, Łojasiewicza 11, Kraków 30-348, Poland*

⁴*Gdańsk University of Technology, Faculty of Electronics, Telecommun. and Informatics, Narutowicza 11/12, 80-233 Gdańsk, Poland*

⁵*University of Warsaw, Faculty of Physics, Pasteura 5, 02-093 Warsaw, Poland*

*alexander.heidt@unibe.ch

Abstract: We present a rapid prototyping method for functionalized silica optical fibers, leveraging laser-assisted preform manufacturing combined with powder-in-tube and sol-gel dip-coating techniques. Laser vitrification enables precise thermal control through an ultra-thin heat blade characterized by localized heating and steep temperature gradients, facilitating high-quality glass formation and the integration of heat-sensitive dopants. We demonstrate three key outcomes: (i) fabrication of Ytterbium-doped active fibers with performance comparable to commercial benchmarks, (ii) development of fibers with fluorescence bandwidths exceeding one octave, doped with multiple rare-earth ions, promising for wide-band telecommunications and ultrashort pulse amplification, and (iii) the first direct doping of silica fibers with nitrogen-vacancy fluorescent nanodiamonds, enabling single-photon quantum emitter integration with the backbone of current information technology networks. Additionally, nanodiamond doping is proposed as a pathway to control the nonlinear refractive index of silica fibers. These findings establish laser-assisted preform fabrication as a versatile and efficient technique for creating advanced optical fibers with innovative functionalities.

© 2025 Optica Publishing Group under the terms of the [Optica Open Access Publishing Agreement](#)

1. Introduction

Optical fibers produced from silica glass have transformed our lives: not only by transmitting information across the globe at the speed of light, but also as integral components in various areas of applications including environmental sensing, medical surgery, and nonlinear optics [1–4]. Unlike telecommunications, where ultra-low loss is the primary requirement, emerging technologies leverage the unique optical, electrical, acoustic, or optoelectronic capabilities of specialty fibers functionalized with passive or active dopant materials such as rare-earth metals, semiconductors, or nanoparticles [5–8].

As the demand for customized specialty fiber grows, standard production methods face challenges. Chemical vapour deposition (CVD) techniques, commonly used to fabricate preforms for drawing silica fibers, are highly effective for cost-efficient large-scale production of high purity silica [9,10]. However, in many research environments the focus lies on producing short sections of highly customized multi-component fibers with novel dopants and functionalities. This process often requires numerous trial-and-error runs to optimize composition and vitrification conditions.

In such situations, CVD methods are often too restrictive in terms of the glass compositions they allow [11], and the running costs and toxic gas emissions can be prohibitive.

The high vitrification temperature of silica glass near 2000°C presents an additional challenge for incorporating novel materials, particularly nanoparticles and 2D materials, as this temperature may compromise their integrity, making post-processing procedures necessary [8,12,13]. Although this temperature challenge can be mitigated by using soft glasses with lower melting temperatures [14], silica fibers remain highly desirable due to their robustness, mechanical and chemical stability, and broad transmission window.

To address these challenges in producing advanced functionalized silica fibers that meet current and future demands, a range of new preform fabrication and drawing techniques have been developed [12,15], with laser-assisted manufacturing attracting particular attention [16–18]. While lasers have long been an integral part of fiber production, primarily serving as heat source for fiber drawing and post-processing [19–21], recent advancements have harnessed their unique capabilities for producing specialty optical fiber preforms. The small and localized hot zone, rapid processing speeds, and high cooling rates achievable with CO₂ lasers, for example, create an intriguing regime for glass making. These conditions minimize the time for potentially detrimental thermal interactions, such as diffusion, dissociation, and oxidation [22], and have been linked to the suppression of concentration quenching and ion clustering at high rare-earth doping levels [18]. Moreover, additive manufacturing techniques such as laser powder deposition hold promise for future 3D printing of highly customized preform rods [23]. However, the technology is still in the proof-of-concept stage, limiting the range of investigated material systems and currently resulting in relatively high losses and low efficiency for rare-earth doped active laser fibers [17,23,24].

In this work, we explore the rapid prototyping of functionalized silica fiber preforms by combining the unique benefits of laser-assisted manufacturing with variations of the established powder-in-tube and sol-gel dip-coating processes. These preform manufacturing techniques have been implemented in various forms [25–29], and are recognized as cost-effective and straightforward methods for obtaining silica glasses doped with a wide range of functional ingredients at high concentrations and uniformity [30–33]. Here, we discuss their implementation using laser-assisted preform fabrication in detail (Section 2), and demonstrate the production of high quality silica fibers with three different functionalizations (Section 3).

We report several key advancements in optical fiber rapid prototyping: (i) production of high-quality glass, exemplified by an Ytterbium-doped fiber with emission characteristics matching state-of-the-art commercial fibers produced using CVD and solution doping techniques; (ii) demonstration of high flexibility through the fabrication of multi-rare-earth-ion-doped fibers with fluorescence bandwidths exceeding one octave; and (iii) introduction of new functionalities via the first successful direct doping of silica fibers with temperature-sensitive nitrogen-vacancy (NV) fluorescent nanodiamonds. These NV-doped fibers are proposed as a novel platform for quantum information processing and for manipulating the nonlinear refractive index of silica fibers. Our findings establish laser-assisted preform fabrication as a viable approach for the rapid prototyping of high-quality optical fibers with unique core compositions. Notably, this method enables the direct incorporation of temperature-sensitive nanomaterials, a capability not achievable with conventional fabrication techniques.

2. Laser-assisted preform fabrication

2.1. Laser system and vitrification setup

Our laser vitrification setup is schematically illustrated in Fig. 1(a). We utilize a multi-kW continuous-wave CO₂ laser system, though only a fraction of its power is required for preform fabrication. The laser emits a circular beam with a $1/e^2$ - diameter of approximately 20 mm and a multimode beam profile ($M^2 \approx 3$) that can be well approximated with a flat-top 4th-order

super-Gaussian. To adjust the dimensions and shape of the hot zone, we employ beam shaping techniques. Since we have ample laser power available, we transform the originally circular laser beam into a nearly rectangular shape by simply passing it through a slit with 9 mm height. We chose a slit over a lens because our kW-class laser requires high output power for stability, and focusing the beam risks excessive preform vaporization or necessitates an attenuator. In contrast, a slit shapes the beam without increasing intensity, making it the more practical option in our case. Figure 1(b) shows the measured beam profiles after the slit and illustrates the derived intensity distribution in relation to a preform tube with 4 mm diameter. The resulting hot zone has a sharp vertical transition between heated and unheated areas, measuring approximately 9 mm in height and 20 mm in width ($1/e^2$ values). Further shaping of the hot zone can be easily achieved using different apertures and lenses as needed.

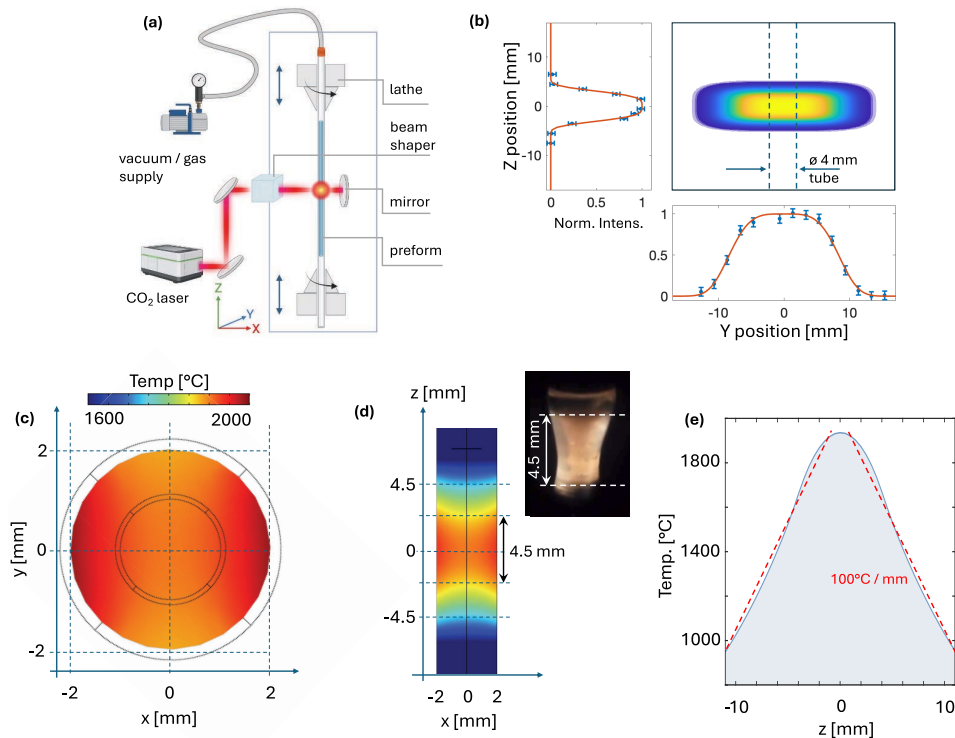


Fig. 1. (a) Schematic of the laser-assisted vitrification setup [34]. (b) Measured beam profiles in parallel (y) and perpendicular (z) direction to the beam-shaping slit (blue dots), fitted with a 4th-order super-Gaussian (red line), and illustration of the derived intensity distribution in relation to a preform tube with 4 mm diameter. The hot zone dimensions are 20×9 mm ($1/e^2$). (c)-(e) Simulated temperature distribution in a pure silica preform with a diameter of 4 mm and a length of 15 cm under bidirectional CO_2 laser irradiation along the x -axis. The beam is centered at $z = 0$, the midpoint of the preform. The maximum surface temperature is set to 2000 °C, preform rotation is not considered. (c) Horizontal cross section at $z = 0$. (d) Vertical cross section at $y = 0$, illustrating the formation of a strongly localized "heat blade" with 4.5 mm height. The inset shows a photograph of the hot zone observed in powder-in-tube laser vitrification (PLV) experiments confirming the simulated dimensions. (e) Vertical temperature distribution at the preform core ($x = y = 0$). A temperature gradient of 100 °C/mm is indicated with the red dashed lines.

As we typically use silica tubes with 5 mm or less outer diameter to produce our preforms, a substantial part of the laser beam passes around the tube. To capture this light and ensure uniform

heat distribution across the tube's cross-section, we employ a retroreflecting cylindrical mirror that redirects the light onto the backside of the tube. In this geometry, a collimated beam after the beam shaper helps to ensure uniform hot zone height. We note that scaling our process to larger-diameter preforms may be challenging due to the limitations of CO₂ laser heating, which relies on surface heating and conduction [35]. As the diameter increases, more power must be deposited to reach core vitrification temperatures. However, the corresponding higher surface temperatures also lead to greater energy losses from convection, emission, and vaporization, ultimately limiting the maximum achievable core temperature. Depending on the vitrification method used (see Sections 2.3 and 2.4), a multi-beam setup, a laser wavelength with deeper penetration, or a combination of both may be necessary for homogeneous heat distribution [21].

A custom-built, computer-controlled vitrification lathe is used to rotate and translate the silica tube vertically along the beam. Depending on the chosen method for producing the preform and the doping materials used, critical vitrification parameters such as laser power, rotational and translational speed are carefully controlled. Gas flow or vacuum can be applied to the preform tube as required. The lathe enables the production of preforms with lengths up to 23 cm.

The preforms are subsequently drawn into fibers using a standard drawing tower, yielding fiber lengths of several hundred meters for a 4 mm diameter preform drawn to a 125 μm diameter fiber. This length is sufficient for research purposes and for developing new fiber compositions and functionalities.

2.2. Heat blade formation

The interaction of CO₂ laser radiation with silica is dominated by surface heating without any substantial absorption of the laser radiation in the bulk of the material due to the low penetration depth [35]. Nevertheless, conductive and radiative transfer from the heated surface to the bulk result in a relatively uniform temperature distribution across the preform's cross section, as confirmed by simulations of the laser heating process using Comsol Multiphysics shown in Fig. 1(c). Considering a pure silica preform with a diameter of 4 mm and a length of 15 cm, a core temperature of 1900°C is reached when the maximum surface temperature is set to 2000°C. The simulations model a static picture of the process, i.e. preform rotation is neglected. The actual temperature distribution with rotation will show stronger rotational symmetry and even better homogeneity.

The vertical temperature distribution along the preform, illustrated in Fig. 1(c) and (d), reveals a strong heat localization within approximately 4.5 mm at the center of the laser beam, with steep temperature gradients on the order of 100°C/mm. The photograph in the inset of Fig. 1(d) shows the hot zone observed in powder-in-tube (PLV) experiments, confirming the simulated dimensions. The hot zone has an "hourglass" shape, with a waist forming as a result of the softening of the powder-filled silica tube in the center of the laser beam.

The formation of a strongly localized hot zone, which we refer to as a "heat blade", is a key feature of the laser vitrification process. As the preform is vertically translated through the beam, each section of the preform is exposed to the high-temperature zone only for a brief period, minimizing potentially harmful thermal interactions, while the rapid subsequent cooling promotes high-quality glass formation. Narrower beams could, in principle, enable even higher heating and cooling rates but introduce a trade-off with surface vaporization and energy loss. The required power to achieve target core temperatures is primarily determined by the preform diameter. Focusing the power into a narrower beam leads to higher surface intensity and temperatures, increasing energy losses from convection and emission, and may cause significant surface vaporization. For our conditions, we found the 9 mm beam height to result in a good compromise between high cooling rates and limited surface vaporization.

2.3. Liquid layer laser vitrification (3LV)

3LV is a variation of the sol-gel dip-coating process [25], and we found it particularly useful for the rapid prototyping of high-quality rare-earth doped fiber preforms for laser and amplifier applications. The basic concept of preform production using 3LV is illustrated in Fig. 2. The doped silica core material is formed by the sequential deposition and CO₂ laser vitrification of multiple thin sol layers inside a fused silica tube. After collapsing the tube, the vitrified layers form the core of the preform, while the silica tube serves as the cladding. This entire procedure, including layer application, vitrification, and preform collapse, can be executed in the laser vitrification machine described in Section 2.1 without needing to move the preform between steps.

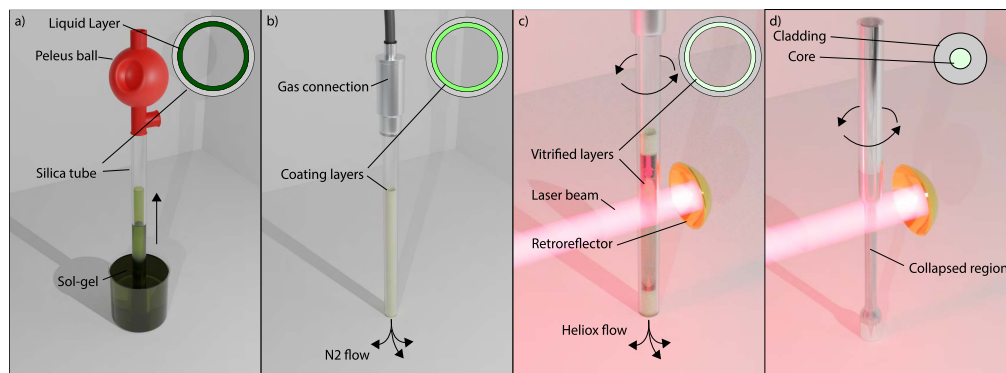


Fig. 2. Schematic of the 3LV process for the production of doped silica fiber preforms. a) Internal dip-coating of a fused silica tube with a thin sol layer containing the dopant precursors. b) Drying under nitrogen atmosphere. c) Laser vitrification of individual layers with heliox flow. d) Collapse of the silica tube. The insets show the cross section of the preform at each step.

The sol is produced by mixing tetraethyl orthosilicate (TEOS) with an ethanol solution of dopants in chloride form at room temperature. A wide variety of functional dopants can be incorporated into the core at high concentrations, maintaining uniformity at the molecular level. Doping with an ethanol suspension of nanoparticles is also possible. The viscosity of the sol, and consequently the thickness of each deposited layer, is adjusted by adding a small amount of distilled water and a few drops of hydrochloric acid. The mixture is stirred overnight to ensure uniform dispersion of SiO₂ precursors and dopants in the liquid phase, resulting in the growth of a homogeneously doped sol-gel matrix.

While the exact process parameters depend on the individual thermodynamic properties of the dopant materials, we provide details on the production of rare-earth doped fiber preforms discussed in Sections 3.1 and 3.2 as a representative example. A thin layer of the sol is applied to the inner surface of a fused silica tube (4 mm outer diameter, 1 mm wall thickness) by creating a weak vacuum to draw the liquid into the tube and then rapidly releasing it, repeating this process twice. The layer is dried for 10 minutes under a steady flow of nitrogen (0.3 l/min) to form a xerogel on the inner wall of the tube. Each layer is then vitrified by setting the CO₂ laser power to 300 W (measured after the beam shaping aperture) while the lathe rotates and translates the tube vertically along the beam at a speed of 12 rpm and 3.6 cm/min, respectively. Thus, each section of the preform is exposed to the hot zone for less than 10 seconds and then rapidly cooled. This speed contributes to the formation of high-quality, crack-free, transparent glass and permits the inclusion of temperature-sensitive materials into the silica glass matrix. A heliox flow (0.5 l/min)

supplies oxygen for calcination and removal of organic impurities during vitrification, while also expelling resultant fumes outward.

The thickness of each layer can be controlled via the viscosity of the sol and lies typically in the order of a few micrometers. This value is sufficiently thin to ensure crack-free layer deposition, effective removal of impurities and the escape of gases during the vitrification process, while also being thick enough to minimize the number of layers needed to build up the core material. Based on our experience and depending on sol viscosity, 1-3 layers are sufficient to build up enough core material for a single-mode fiber core. Since applying each layer only takes 25 minutes, the entire preform can be fabricated within a couple of hours.

Finally, the tube is collapsed by reducing the laser power to 250 W and using a slower translation speed of 1.44 cm/min and 40 rpm, without applying gas flow or vacuum. This step is highly sensitive to pressure differences, which can cause deformations in the preform. Therefore, it is best to leave both ends of the tube open to achieve a symmetric collapse. The fiber can be drawn directly from the preform without needing additional cladding tubes.

2.4. Powder-in-tube laser vitrification (PLV)

PLV is derived from the powder-in-tube process, which has been explored in various forms capitalizing on its advantages, such as the ability to fabricate arbitrary shapes and produce thick preforms with high dopant uniformity—capabilities that are challenging to achieve with CVD methods. Here, we adapt it in a straightforward manner for rapid prototyping of fiber preforms using laser vitrification. We found the PLV process particularly useful for the integration of nanoparticles into a pure silica fiber core. Section 3.3 discusses the production of a nanodiamond doped silica fiber as an example. While it is also possible to incorporate active rare-earth elements using this method, as demonstrated with a multi-dopant fiber in Section 3.2, we observed a strong tendency for micro-bubble formation during vitrification, resulting in high scattering losses and unsatisfactory glass quality. Based on our experience, the 3LV method is better suited for producing high-quality, bubble-free preforms doped with active rare-earth elements.

Unlike the 3LV process, which involves the sequential vitrification of multiple thin layers, the PLV approach is essentially a one-step vitrification process, as schematically summarized in Fig. 3. The doped silica core material is prepared in powder form and filled into a fused silica tube that has been collapsed at its lower end, forming a powder column that fills the entire central void of the tube. The tube is connected to a vacuum system and may undergo a preheating process to remove impurities from the powder production process. The powder is then vitrified with a single pass of a CO₂ laser, completing the production of the core rod.

For preparing the doped core material, granulated silica powder and the desired nanoparticle dopants are suspended in ethanol, combined, and continuously stirred while the ethanol evaporates under constant heating at 80°C. Dopants for adjusting the refractive index, such as aluminum, or active rare-earth elements may be added to the suspension in the form of their chloride salts. Mixing in liquid suspension aims to achieve a homogeneously doped silica powder, where the dopants are adsorbed onto the pores at the surface of the silica granulate. Thus, unlike the 3LV method, which achieves homogeneous doping distribution down to the molecular level, the PLV process retains a certain degree of inhomogeneity at the scale of a single granulate particle.

The resulting dried powder is filled into a fused silica tube (typically 4 mm in diameter, 1 mm wall thickness, 20 cm height of the powder column) and preheated overnight at temperatures between 300–800°C under vacuum, depending on the chosen doping material. This can be done using either a tube furnace or low-power scanning laser irradiation to remove any remaining moisture and organic impurities from the powder production process. The preheating is concluded when the vacuum pressure drops to approximately 3×10^{-3} mbar, close to the final pressure achievable with the vacuum pump, indicating no further outgassing from the powder. Without interrupting the vacuum, the tube containing the doped powder is vitrified using the laser



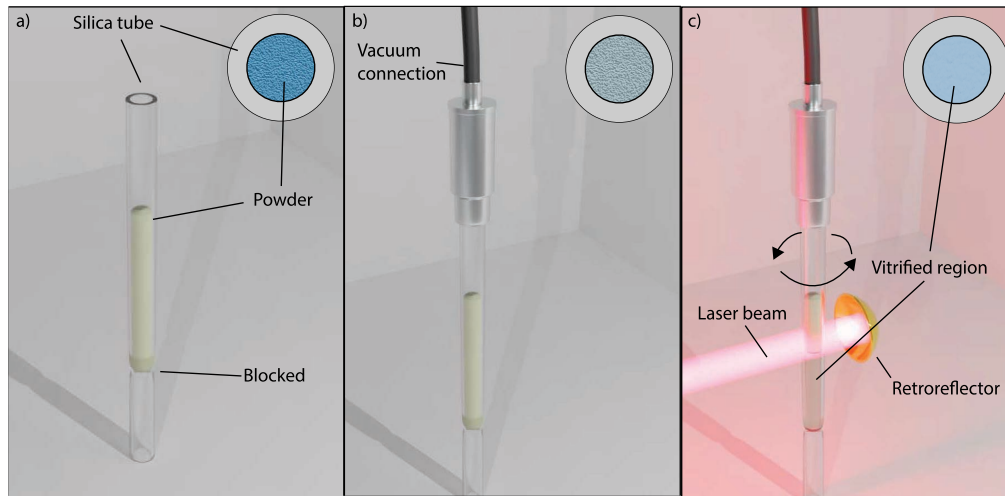


Fig. 3. Illustration of the PLV process for the production of doped silica fiber preforms. a) Filling of a fused silica tube with powder containing the doped core material. b) Evacuation and pre-heating. c) Laser vitrification of the preform. The insets show the cross section of the preform at each step.

vitrification setup described in Section 2.1. The vertical translation speed of the lathe is set to a few mm/s, much slower than the 3LV method, to allow any fumes emitted during the powder melting and vitrification process to escape upwards through the dense powder column and avoid the formation of gas bubbles in the vitrified rod.

Since the PLV method yields preforms with a relatively large core diameter, jacketing the core rod with cladding tubes is necessary for drawing single-mode fibers.

On a final note, it is worth highlighting that the small hot zone of laser vitrification and the ease of stacking powders in a single preform enable rapid screening of different doping compositions and vitrification parameters during a single run, simplifying any optimization processes that would be necessitated by specific glass compositions.

3. Example fibers

In this section, we examine three different functionalizations of silica fibers fabricated with the 3LV and PLV methods. First, we present an ytterbium (Yb) / aluminum (Al) co-doped silica fiber, designed as an active gain medium in a fiber laser emitting at 1 μm wavelength, and demonstrate that its absorption and emission characteristics are on par with state-of-the-art commercial Yb-doped fibers fabricated with conventional CVD/solution doping techniques. Second, we showcase the versatility of our laser-assisted preform fabrication approach by introducing fibers doped with multiple active rare-earth ions, achieving fluorescence bandwidths that exceed one octave. Third, we describe the functionalization of a silica preform and fiber with nitrogen-vacancy (NV) fluorescent nanodiamonds, proposing this as a novel approach for controlling the nonlinear refractive index of silica fibers.

3.1. Yb-doped aluminosilicate fiber

Production. The preform is produced using the 3LV process described in Section 2.3, utilizing a fused silica tube with a 4 mm outer diameter and 1 mm wall thickness, and applying five deposited layers. The target final ratio of relevant dopant ions in the SiO_2 matrix was 1 at.% Yb^{3+} and 10 at.% Al^{3+} .

To produce 50 mL of sol, we dissolved 0.29 g of $\text{YbCl}_3 \cdot 6\text{H}_2\text{O}$ (99.998%, Sigma-Aldrich) and 1.8 g of $\text{AlCl}_3 \cdot 6\text{H}_2\text{O}$ (99.998%, Sigma-Aldrich) in 33.8 mL of absolute ethanol (EMSURE, Sigma-Aldrich). Once the salts were fully dissolved, 14.7 mL of TEOS (for synthesis, 99%, Sigma-Aldrich) was added. The viscosity of the sol, and consequently the thickness of each deposited layer, was adjusted by adding a small amount of distilled water (1.48 mL) and hydrochloric acid (7 μL , 37 wt.%, Dr. Grogg Chemie AG).

The cross-section of the resulting collapsed preform is shown in Fig. 4(a). Based on its dimensions and using the principle of mass conservation, we estimate the thickness of each deposited layer before collapse to be 9.4 μm . The preform was then drawn to a fiber diameter of 130 μm in a standard drawing tower. A commercial high-index acrylate coating was applied for increased mechanical stability. A microscope image of the cleaved front facet of the final fiber, named YbDF2, is shown in Fig. 4(b), confirming good concentricity.

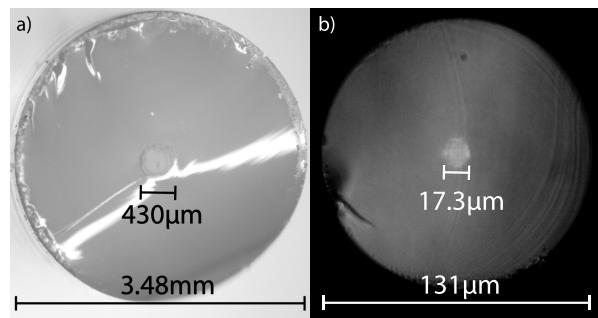


Fig. 4. Micrographs of the Yb-doped preform fabricated using the 3LV process (a) and the drawn fiber (b), back-illuminated with white light.

Refractive index and doping concentration. The concentration of dopants in the fabricated fiber core was determined using energy-dispersive x-ray spectroscopy (EDX), revealing a composition of 0.5 at.% Yb and 7.7 at.% Al, referenced to Si. This corresponds to an Yb ion number density of approximately $1.23 \times 10^{20} \text{ cm}^{-3}$. Compared to the chemical composition of the sol, the Yb doping concentration in the fiber core decreases to approximately half its initial value. This result is not an artifact of EDX measurement uncertainty, which we estimate to $< 10\%$ of the reported mean values, but is independently verified using the relationship between doping concentration and refractive index change Δn established in [36]. Based on EDX data and the additivity rule linking Δn to Yb content and co-dopant concentrations, the expected Δn is 0.0106, which aligns well with the experimental value of $\Delta n = 0.0103$ obtained from refractive index profiling discussed below. This finding is further supported by our earlier work, which showed that diffusion of Si from the cladding into the core during fiber drawing can significantly reduce dopant concentrations [37].

Diffusion effects at the core/cladding interface influencing the doping distribution are also evident in the measured refractive index profile in Fig. 5, which has a parabolic shape near the center of the core, and small pedestals reaching into the cladding. A similar refractive index profile shape was observed in a commercial Yb-doped fiber used as a reference, indicating that this phenomenon is inherent to the high-temperature drawing process of silica fibers rather than specific to a particular preform fabrication method. The core exhibits a maximum index step of $\Delta n = 0.0103$, corresponding to a numerical aperture of $\text{NA} = 0.174$. The core diameter, defined at the 5% height of the maximum index step, measures approximately 17.3 μm . Using a numerical mode solver with the measured refractive index profile, ten guided mode solutions were identified. The calculated mode-field diameter of the fundamental mode at 1030nm is approximately 8.4 μm . Note that obtaining single-mode guidance in the fiber was not an objective of this study.

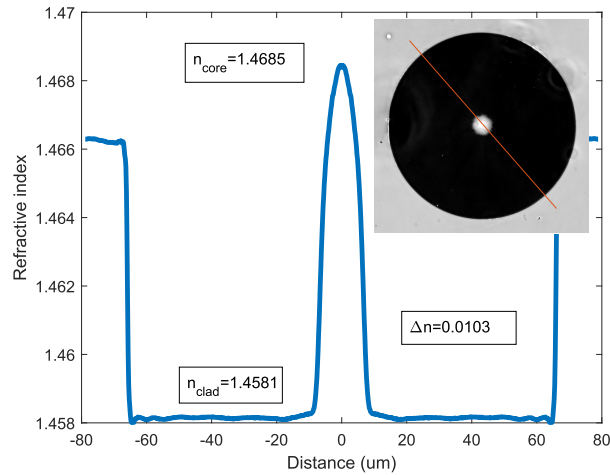


Fig. 5. Refractive index line profile of the YbDF2 fiber measured with a commercial instrument (nPA-600, Arden Photonics, UK). The inset shows the two-dimensional profile, the red line indicates the orientation of the shown line profile.

Absorption and emission characteristics. The fabricated fiber was subjected to a series of optical characterization measurements to evaluate its absorption and emission properties, and its performance was benchmarked against a state-of-the-art commercial Yb-doped fiber. As reference, we selected Coherent YSF-HI-HP since it is a widely used single-clad fiber for laser and amplifier systems with relatively high doping concentration [38]. Using EDX we determined a composition of (0.17 ± 0.03) at.% Yb, (5.0 ± 0.5) at.% Al, and (1.0 ± 0.1) at.% P for the Coherent YSF, which corresponds to about one third of the Yb doping level of our in-house fabricated YbDF2 fiber.

Figure 6(a) shows the measured absorption spectra of both fibers. To accurately resolve the strong absorption peak around 976 nm, we employed the fiber pinhole technique as described in [39]. This method involves splicing a short piece (approx. 1 cm) of the fiber under test (FUT) between two passive PM980 fibers. These passive fibers act as pinhole fibers, ensuring that light is coupled into and collected from the fiber core only. The shape of the absorption spectrum is then easily obtained by comparing the white-light transmission spectra recorded with the FUT and the pinhole fibers alone. The absolute values were calibrated using a single-wavelength cut-back measurement at 895 nm, where the lower absorption permits longer cut-backs and more accurate measurements. For the Coherent YSF reference fiber, peak absorption values of 80 dB/m at 915 nm and 247 dB/m at 976 nm are determined, in excellent agreement with the manufacturer specifications [38]. The YbDF2 fiber exhibits significantly higher absorption, with peak values of 208 dB/m at 915 nm and 925 dB/m at 976 nm, reflecting its approximately threefold higher doping concentration. The background loss of the fiber outside of the absorption bands was characterized with a cut-back measurement at 640 nm, resulting in a loss of 0.5 dB/m, which is line with Yb-doped aluminosilicate fibers produced by MCVD and solution doping [40].

Fluorescence characteristics were evaluated by exciting a short length of the FUT directly spliced to a single-mode 976 nm laser diode and measuring the fluorescence signal perpendicular to the fiber immediately after the splice to minimize reabsorption effects along the fiber path [39]. Fluorescence lifetime measurements were performed by modulating the diode with a square wave signal at a few Hz repetition rate and a 50% duty cycle. The pump level was set above the saturation intensity of the respective fiber, and no spectral filter was used. The results (Fig. 6(b)) reveal single exponential decays with nearly identical lifetimes of 820 μs for

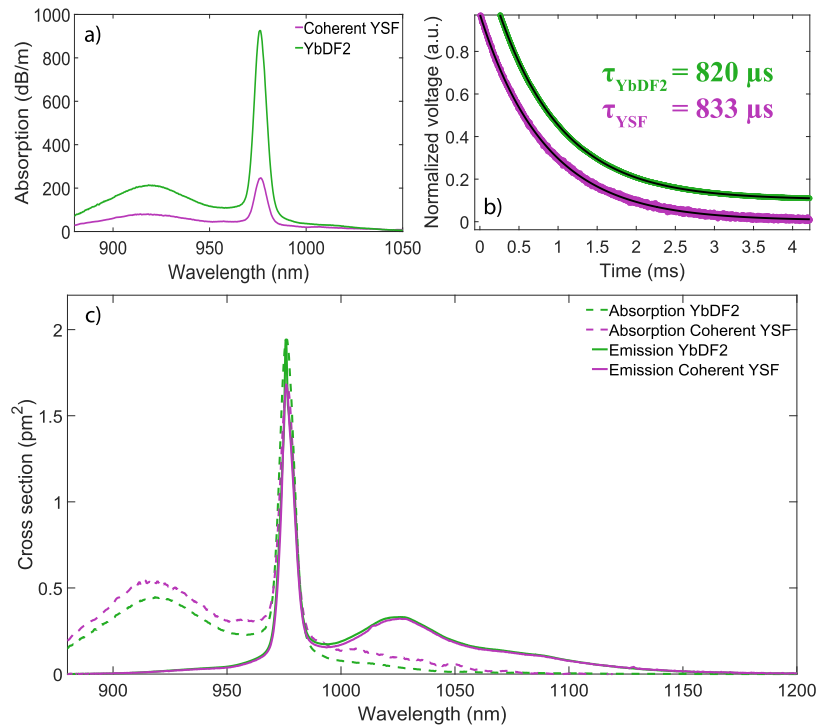


Fig. 6. Measured absorption and emission characteristics of our YbDF2 fiber benchmarked against a commercial Yb-doped fiber (Coherent YSF-HI-HP). (a) Absorption spectra. (b) Fluorescence lifetimes (offset for clarity). (c) Absorption and emission cross sections.

YbDF2 and 833 μs for Coherent YSF. This result shows that our process produces doped glass of comparable quality to a commercial sample. Despite a threefold higher doping concentration, the Yb ions are well-integrated into the silica matrix, with no evident signs of concentration quenching or clustering.

Finally, absorption and emission cross sections were calculated from the measured attenuation and fluorescence characteristics, the Yb ion densities determined by EDX, and the measured refractive index profiles of both fibers [41]. Cross sections reflect the efficiency of absorption and emission processes at the level of individual ions, independent of the fiber's geometrical design and doping concentration, and are therefore effective indicators for the quality of the doped glass material. Figure 6(c) compares the results for YbDF2 and Coherent YSF fibers. We observe distinct performances of the fibers at the two primary absorption peaks. The YSF fiber shows a higher cross section at 915 nm, whereas our YbDF2 fiber exhibits a more pronounced peak at 976 nm. These variations can be attributed to differences in glass composition, such as the presence of additional phosphor co-doping in the YSF fiber, as indicated by our EDX measurements. Uncertainties in absorption measurements at high doping concentrations might also contribute to this result. In contrast, the important emission cross sections at and above 1030 nm are nearly identical for both fibers. This outcome highlights that fibers produced with our laser-assisted rapid prototyping approach exhibit emission characteristics on par with commercial fibers fabricated using conventional CVD/solution doping techniques.

Laser experiment. For evaluating the continuous-wave (CW) lasing performance of the YbDF2 fiber, we constructed the Fabry-Perot test cavity shown in Fig. 7(a). A single-mode pigtailed pump diode operating at 976 nm and a 19 cm length of YbDF2 fiber were spliced to the pump and common port of a wavelength-division multiplexer (WDM), respectively. A mode-field

adapter fabricated from ultra-high numerical aperture fiber (UHNA7, Coherent) was used to limit the transmission loss between the single-mode WDM pigtail and the multi-mode YbDF2 fiber to 10% [42]. The resonator is formed by a 100% reflecting silver mirror butt-coupled to the signal port of the WDM and the cleaved end facet of the YbDF2 fiber, which results in about 4% Fresnel reflectivity.

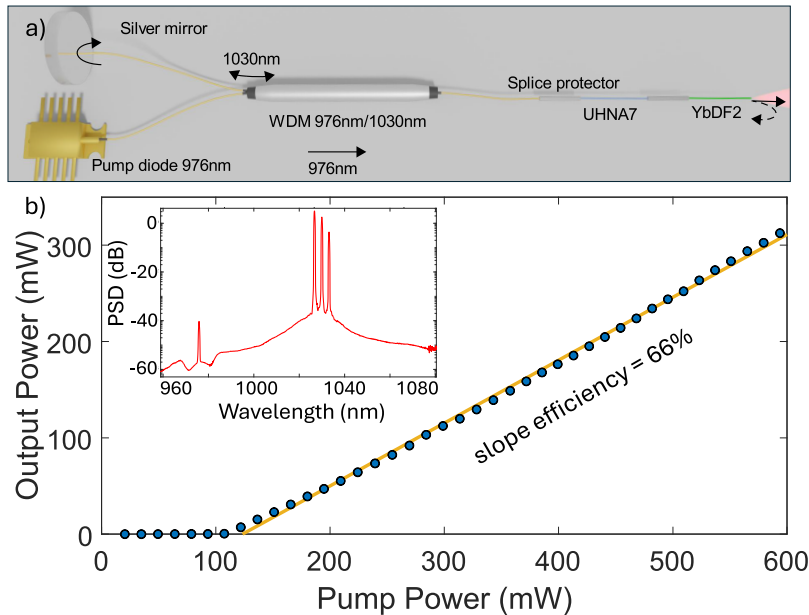


Fig. 7. (a) Schematic of the Yb-doped fiber laser arrangement. The cavity is formed between the silver mirror and the cleaved fiber facet. UHNA7 fiber serves as mode-field adapter between the single-mode passive fibers and the multi-mode active YbDF2 fiber. (b) Output power as a function of absorbed pump power. The inset shows the optical spectrum of the laser emission.

Figure 7(b) shows the lasing characteristics of the YbDF2 fiber in an output power range up to 310 mW, limited by pump power. The slope efficiency with respect to absorbed pump power was determined to be about 66%, which is an excellent value considering the mode-mismatch and excess loss in the cavity. As expected from a free-running laser, a multi-peak emission spectrum was recorded near the gain maximum of 1030 nm as shown in the inset of Fig. 7(b).

3.2. Multiple rare-earth dopants

To demonstrate the flexibility of our laser-assisted rapid-prototyping process, we fabricated fibers with fluorescence bandwidth exceeding one octave in the near-infrared spectral region by doping with multiple active rare-earth ions. These fibers are potentially useful as ultra-broadband superluminescent light sources, combining the high spatial coherence of single-mode fibers with very low temporal coherence resulting from the large emission bandwidth [43,44]. This unique combination of low temporal and high spatial coherence is particularly advantageous for applications in optical coherence tomography, device characterization, and optical sensing [45].

Additionally, multi-dopant fibers present a promising solution for overcoming the gain bandwidth limitations inherent in fiber amplifiers that rely on a single active dopant. By incorporating multiple dopants with adjacent gain bands, these fibers can potentially expand the useful transmission bandwidth of telecommunication networks [46]. Moreover, they could

enable new possibilities in the amplification of few-cycle pulses, which are essential for various advanced applications in ultrafast optics and high-precision measurements [47].

For this demonstration, we produced two multi-dopant fibers, one using 3LV and the other using the PLV process, labeled MD-3LV and MD-PLV, respectively. The doping compositions were chosen to combine several active rare-earth elements with emission bandwidths in the near-infrared region: Ytterbium (Yb; 1.0-1.1 μm), Neodymium (Nd; 0.9 – 0.95 μm , 1.03 - 1.1 μm , and 1.32 - 1.35 μm), Bismuth (Bi; 1.1-1.5 μm), Erbium (Er; 1.5-1.6 μm), Thulium (Tm, 1.45 - 1.53 μm and 1.7 – 2.1 μm), and Holmium (Ho, 2.1 μm). The solubility of the ions in the silica glass matrix was ensured by co-doping with aluminum. The detailed composition of both fiber cores are given in Table 1.

Table 1. Core doping concentrations for MD-3LV and MD-PLV fiber samples, and emission bands for each active rare-earth dopant.

	Yb	Er	Tm	Ho	Nd	Bi	Al
MD-3LV (at.%)	0.19	0.13	0.26	-	-	-	5.03
MD-PLV (at.%)	0.06	0.06	0.06	0.06	0.06	1.2	3
Emission wavelength (μm)	1.0-1.1	1.5-1.6	1.45-1.53 1.7-2.1	2.1	0.9-0.95 1.03-1.1 1.35-1.45	1.1-1.5	-

Fluorescence spectra, recorded in transmission at the end of the fiber samples, are shown in Fig. 8. Both fiber samples exhibit a fluorescence bandwidth exceeding one octave using a single pump wavelength, but important differences exist as a result of the core glass compositions.

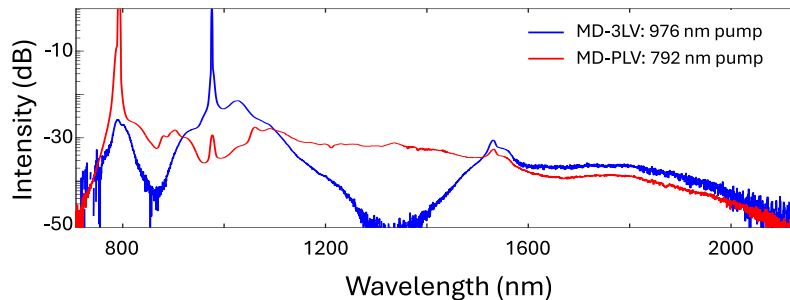


Fig. 8. Broadband luminescence from silica fibers doped with multiple rare-earth elements. The MD-3LV fiber contains Yb, Er, and Tm ions as active doping materials and is pumped at 976 nm. The MD-PLV fiber contains additional Nd and Bi doping, leading to a continuous emission spectrum when pumped at 792 nm.

The MD-3LV fiber was pumped with a 976 nm laser diode, ensuring that most of the pump light is absorbed by the Yb ions, subsequently transferring energy to Er and Tm ions through a mechanism similar to that in Er-Yb co-doped fibers [48]. Three distinct emission bands are observed, centered at 1.03 μm , 1.53 μm , and 1.9 μm , corresponding to Yb, Er, and Tm ions, respectively. A gap in the spectrum is noted around 1.3 μm , where none of the dopants exhibit fluorescence emission.

Pumping with a 792 nm laser diode is more appropriate for the MD-PLV fiber composition, which includes additional Nd and Bi doping. This results in a smooth, continuous fluorescence spectrum spanning 900–2100 nm. Nd emission in the 1350–1450 nm range partially bridges the gap between Yb and Er, while Bi closes the remaining 1150–1350 nm gap and enhances

emission in the 1350–1500 nm range. The contributions of Nd and Bi to the overall emission spectrum were validated through separate experiments using fibers with varying compositions. Due to the complexity of the core composition, the exact excitation mechanism for all dopants is unknown. The 792 nm pump light can be directly absorbed by Nd, Bi, and Tm ions, bringing them into their excited states. It is likely that from there energy transfer as well as emission and reabsorption processes take place that result in the simultaneous excitation of all active dopants and the formation of the continuous fluorescence spectrum.

These proof-of-concept experiments demonstrate the possibility of obtaining broadband emission from a single silica fiber doped with multiple rare-earth elements. In this demonstration, we aimed to show that laser-assisted vitrification addresses two key challenges in multi-dopant active fiber development: nonradiative quenching and the chemical compatibility needed for incorporating multiple rare-earth dopants. Bi and Nd co-doping effectively closes the 1.3 μm gap between Yb and Er emission, while Al co-doping enhances dopant solubility. While these strategies are well-established, laser-assisted vitrification significantly reduces fabrication costs, making iterative optimization of dopant compositions practical even for fiber-grade silica glass. It is clear that the core composition, the balance of doping concentrations, and the pumping scheme are key factors influencing the emitted spectrum's shape and the efficiency of the excitation processes. Producing a range of fibers with variations in these parameters will be required to understand the complex interactions between dopants and to obtain a fiber suitable for wide-band amplification of light. The laser-assisted rapid prototyping techniques presented in this manuscript are well suited for this purpose.

3.3. Nanodiamond doping

Controlling nonlinear processes is important for a broad range of applications, including telecommunications, ultrafast photonics, and biophotonic imaging [49]. The dominant optical nonlinearities in silica fibers are induced by the nonlinear Kerr effect, which describes an intensity-dependent refractive index, $n(I) = n_0 + n_2I$, where n_0 and n_2 represent the linear and nonlinear refractive indices, respectively [50].

Traditionally, n_2 has been considered a near-constant material property. Altering its magnitude typically required changing the host material, which often leads to handling and system integration challenges [51].

Nanoparticle doping is a promising approach to control n_2 by introducing small amounts of highly nonlinear dopant materials while maintaining silica as the host [52–54]. Nanodiamonds, in particular, are of interest as they can exhibit a negative n_2 value [55,56], which could potentially reduce or even neutralize the positive Kerr nonlinearity of silica glass. Numerical studies have emphasized the significant implications of this additional degree of freedom in designing fiber nonlinearities, especially for applications in ultrafast photonics [57–59]. However, the low dissociation temperature of nanodiamonds, around 600°C, has thus far prevented the development of ND-doped silica fibers, confining previous studies to soft-glass materials with lower melting points, such as tellurite and silicate glasses [14,60,61]. The high optical attenuation and - in the case of tellurite glass - the significantly greater nonlinearity compared to silica have, to date, hindered the observation of any impact of ND doping on the n_2 value of the resulting fiber. The laser-assisted vitrification approach facilitated significant progress in this regard, leading to the first demonstration of optical-quality silica glass bulk samples with nanodiamonds incorporated into the glass matrix. A detailed discussion on the physics of how this nanodiamond incorporation affects nonlinear refraction and nonlinear absorption in the developed glass preforms was provided in our previous work [62].

Here, we go beyond those results, demonstrating that the unique capabilities of laser-assisted preform development enable the drawing of ND-doped silica fibers despite the high processing temperatures. A reduction of the n_2 value is observed in the ND-doped preform core, and



the attenuation of the fabricated fibers is shown to be sufficiently low to allow for nonlinear characterization experiments.

Production. The preform for the ND-doped silica fiber was fabricated using the PLV process described in Section 2.4. Fluorescent nanodiamond particles (NDNV140nmHi, Adamas Nanotechnologies, USA), with a mean diameter of 180 nm and containing negatively charged nitrogen-vacancy (NV) color centers, were chosen to facilitate the identification of nanodiamonds in the fabricated preforms. Granulated silica powder and nanodiamonds at a concentration of 10 μg per 1 g of silica (10 ppm) were suspended in ethanol. This mixture was continuously stirred while the ethanol was evaporated under constant heating at 80°C.

The resulting dried powder was then filled into a silica tube (4 mm outer diameter, 1 mm wall thickness) preheated at a maximum temperature of 600°C. Compared to the vitrification of a pure silica preform with the same dimensions, we found that a significant reduction of laser power by nearly 50% to 175 W and a relatively fast translation speed of 1.44 mm/min were necessary to obtain preforms without visible defects. We attribute this to the high thermal conductivity of nanodiamonds and the associated changes in the thermodynamic properties of the silica/ND hybrid core material. Importantly, the fiber drawing was performed at a standard silica fiber drawing tower without any modifications to the usual drawing protocols. This highlights the robustness of laser-assisted vitrification, even for the fabrication of highly exotic dopant compositions.

Preform and fiber characterization. The survival of nanodiamonds in the preform was confirmed using confocal microscopy on a polished 2 mm thick disk cut from the preform. Fluorescence from the NV color centers with its characteristic spectral shape was observed in the core region under 532 nm laser excitation, as shown in Fig. 9. The reduced laser power, the small hot zone, and the limited heat exposure time are likely contributing factors to a significant fraction of nanodiamonds surviving the preform fabrication process, despite the high-temperature environment required for silica vitrification.

Further characterization of the nonlinearity of the fabricated preform using the z-scan technique revealed a 20% reduction in the magnitude of n_2 compared to a pure silica reference sample fabricated using the same technique [62]. The value of n_2 decreased from $n_2 = 2.3 \times 10^{-20} \text{ m}^2/\text{W}$ for the pure silica preform to $n_2 = 1.8 \times 10^{-20} \text{ m}^2/\text{W}$ for the ND-doped preform, measured at 1030 nm.

Since ND doping is not expected to significantly change the refractive index of the core, the preform was first jacketed with a low-index fluorine-doped cladding tube to form a light-guiding structure, followed by a pure silica cladding tube to adjust the final core-cladding ratio of the fiber, which was drawn in a standard silica drawing tower.

The refractive index profiles of the fabricated fiber, shown in Fig. 9(c) and (d), confirm that the core index remains unchanged by ND doping, matching the refractive index of the outer pure silica cladding. The $\text{NA} \approx 0.1$ is defined by the index step to the fluorine-doped silica cladding, and the core diameter is approximately 10 μm .

As the presence of nanoparticles may result in scattering losses, the attenuation of the fiber was measured using the cut-back technique at 976 nm, resulting in a value of 0.145 dB/m. These losses are orders of magnitude lower than those reported for ND-doped soft-glass fibers [14] and well-suited for further nonlinear characterization of the fiber. These experiments are currently ongoing, and the results will be discussed in future works.

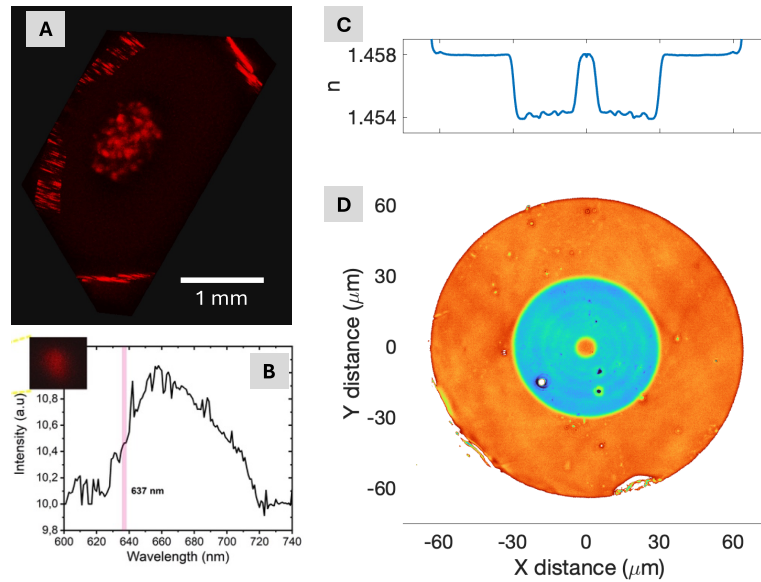


Fig. 9. Characterization of nanodiamond-doped silica preform and fiber. (a) Confocal microscopy image of a thin disk cut from the preform, showing fluorescence from the NV color centers in the core region under 532 nm laser excitation. (b) Characteristic spectrum of a single NV center emission. (c) Refractive index line profile and two-dimensional profile (d) of the fabricated nanodiamond-doped fiber, measured with a commercial instrument (nPA-600, Arden Photonics, UK)

4. Conclusion

We present a novel method for rapid prototyping of high-quality functionalized silica optical fibers using laser-assisted preform manufacturing combined with powder-in-tube and sol-gel dip-coating processes. The laser vitrification process generates an ultra-thin heat blade, enabling precise heat localization and steep temperature gradients, which minimize harmful thermal effects and allow the incorporation of heat-sensitive dopant materials.

The method was validated by fabricating an Yb/Al co-doped gain fiber with threefold higher doping concentration than a state-of-the-art commercial benchmark, demonstrating identical upper-state lifetimes and similar emission/absorption cross-sections. This confirms the production of high-quality doped glass with minimal clustering or quenching effects. The process complements established fabrication methods, such as MCVD, in that it enables the rapid exploration of new chemical compositions and dopants in a research environment, which might later be transferred to MCVD technology to scale up production or chemical purity.

The process's flexibility was showcased by producing multi-rare-earth-ion-doped fibers with fluorescence bandwidths exceeding one octave in the near-infrared. These fibers have potential for overcoming the gain bandwidth limitations of traditional amplifiers, enhancing telecom bandwidths, and advancing ultrashort pulse amplification, though further optimization is required to refine dopant interactions.

For the first time, the method enabled direct doping of silica fibers with temperature-sensitive nanodiamonds, confirmed by detecting the characteristic emission from embedded fluorescent nitrogen-vacancy color. This innovation integrates single-photon quantum emitters into optical fibers, advancing quantum-classical photonic interfaces. Additionally, nanodiamond doping significantly altered the nonlinear refractive index of the preforms, suggesting potential for novel nonlinear and ultrafast photonic devices.

This work establishes laser-assisted preform manufacturing as a versatile and efficient technique for creating advanced silica fibers with functionalities that are challenging or unattainable using conventional methods.

Funding. Schweizerischer Nationalfonds zur Förderung der Wissenschaftlichen Forschung (PCEFP2_181222); Fundacja na rzecz Nauki Polskiej (TEAM NET POIR.04.04.00-00-1644/18, POIR.04.02.00-00-495 D001/20).

Acknowledgments. The authors thank Arden Photonics, UK, for providing fiber refractive index measurements.

Disclosures. The authors declare no conflicts of interest.

Data availability. Data underlying the results presented in this paper are available in Ref. [63].

References

1. C. K. Kao, "Nobel lecture: Sand from centuries past: Send future voices fast," *Rev. Mod. Phys.* **82**(3), 2299–2303 (2010).
2. A. Rampur, D.-M. Spangenberg, B. G. A. Sierro, *et al.*, "Perspective on the next generation of ultra-low noise fiber supercontinuum sources and their emerging applications in spectroscopy, imaging, and ultrafast photonics," *Appl. Phys. Lett.* **118**(24), 240504 (2021).
3. P. Lu, N. Lalam, M. Badar, *et al.*, "Distributed optical fiber sensing: Review and perspective," *Appl. Phys. Rev.* **6**(4), 041302 (2019).
4. G. Keiser, F. Xiong, Y. Cui, *et al.*, "Review of diverse optical fibers used in biomedical research and clinical practice," *J. Biomed. Opt.* **19**(8), 080902 (2014).
5. G. Loke, W. Yan, T. Khudiyev, *et al.*, "Recent progress and perspectives of thermally drawn multimaterial fiber electronics," *Adv. Mater.* **32**(1), 1904911 (2020).
6. U. J. Gibson, L. Wei, and J. Ballato, "Semiconductor core fibres: materials science in a bottle," *Nat. Commun.* **12**(1), 3990 (2021).
7. J. Ballato and A. C. Peacock, "Perspective: Molten core optical fiber fabrication—a route to new materials and applications," *APL Photonics* **3**(12), 120903 (2018).
8. W. Blanc, Z. Lu, T. Robine, *et al.*, "Nanoparticles in optical fiber, issue and opportunity of light scattering [invited]," *Opt. Mater. Express* **12**(7), 2635 (2022).
9. S. Nagel, J. MacChesney, and K. Walker, "An overview of the modified chemical vapor deposition (MCVD) process and performance," *IEEE J. Quantum Electron.* **18**(4), 459–476 (1982).
10. J. E. Townsend, S. B. Poole, and D. N. Payne, "Solution-doping technique for fabrication of rare-earth-doped optical fibres," *Electron. Lett.* **23**(7), 329–331 (1987).
11. J. Ballato and P. Dragic, "Rethinking optical fiber: New demands, old glasses," *J. Am. Ceram. Soc.* **96**(9), 2675–2692 (2013).
12. J. Ballato, H. Ebindorff-Heidepriem, J. Zhao, *et al.*, "Glass and process development for the next generation of optical fibers: A review," *Fibers* **5**(1), 11 (2017).
13. G. Q. Ngo, E. Najafidehaghani, Z. Gan, *et al.*, "In-fibre second-harmonic generation with embedded two-dimensional materials," *Nat. Photonics* **16**(11), 769–776 (2022).
14. M. R. Henderson, B. C. Gibson, H. Ebindorff-Heidepriem, *et al.*, "Diamond in tellurite glass: a new medium for quantum information," *Adv. Mater.* **23**(25), 2806–2810 (2011).
15. J. Ballato and P. D. Dragic, "Glass: The carrier of light—part II—a brief look into the future of optical fiber," *Int. J. Appl. Glass Sci.* **12**(1), 3–24 (2021).
16. W. Zhang, J. Wu, G. Zhou, *et al.*, "Yb-doped silica glass and photonic crystal fiber based on laser sintering technology," *Laser Phys.* **26**(3), 035801 (2016).
17. P. Maniewski, C. M. Harvey, K. Mühlberger, *et al.*, "Rapid prototyping of silica optical fibers," *Opt. Mater. Express* **12**(7), 2426 (2022).
18. P. Maniewski, T. J. Wörmann, V. Pasiskevicius, *et al.*, "Advances in laser-based manufacturing techniques for specialty optical fiber," *J. Am. Ceram. Soc.* **107**(8), 5143–5158 (2024).
19. U. C. Paek, "Laser drawing of optical fibers," *Appl. Opt.* **13**(6), 1383 (1974).
20. A. Heptonstall, M. A. Barton, A. Bell, *et al.*, "Invited article: CO₂ laser production of fused silica fibers for use in interferometric gravitational wave detector mirror suspensions," *Rev. Sci. Instrum.* **82**(1), 011301 (2011).
21. C. M. Harvey, K. Mühlberger, T. Oriekhov, *et al.*, "Specialty optical fiber fabrication: fiber draw tower based on a CO laser furnace," *J. Opt. Soc. Am. B* **38**(12), F122 (2021).
22. T. Oriekhov, C. M. Harvey, K. Mühlberger, *et al.*, "Specialty optical fiber fabrication: preform manufacturing based on asymmetrical CO laser heating," *J. Opt. Soc. Am. B* **38**(12), F130 (2021).
23. Y. Luo, J. Canning, J. Zhang, *et al.*, "Toward optical fibre fabrication using 3D printing technology," *Opt. Fiber Technol.* **58**, 102299 (2020).
24. P. Maniewski, M. Brunzell, L. Barrett, *et al.*, "Er-doped silica fiber laser made by powder-based additive manufacturing," *Optica* **10**(10), 1280 (2023).
25. K. Susa, I. Matsuyama, S. Satoh, *et al.*, "New optical fibre fabrication method," *Electron. Lett.* **18**(12), 499–500 (1982).



26. F. Wu, G. Puc, P. Foy, *et al.*, “Low-loss rare earth doped single-mode fiber by sol-gel method,” *Mater. Res. Bull.* **28**(7), 637–644 (1993).
27. M. Leich, F. Just, A. Langner, *et al.*, “Highly efficient Yb-doped silica fibers prepared by powder sinter technology,” *Opt. Lett.* **36**(9), 1557 (2011).
28. U. Pedrazza, V. Romano, and W. Lüthy, “Yb³⁺, Al³⁺ sol-gel silica glass fiber laser,” *Opt. Mater.* **29**(7), 905–907 (2007).
29. Y. Li, J. Huang, Y. Li, *et al.*, “Optical properties and laser output of heavily Yb-doped fiber prepared by sol-gel method and DC-RTA technique,” *J. Lightwave Technol.* **26**(18), 3256–3260 (2008).
30. V. Matějček, I. Kašík, D. Berková, *et al.*, “Sol-gel fabrication and properties of silica cores of optical fibers doped with Yb³⁺, Er³⁺, Al₂O₃ or TiO₂,” *J. Sol-Gel Sci. Technol.* **13**(1/3), 617–621 (1998).
31. M. Neff, V. Romano, and W. Lüthy, “Metal-doped fibres for broadband emission: Fabrication with granulated oxides,” *Opt. Mater.* **31**(2), 247–251 (2008).
32. G. Granger, C. Restoin, P. Roy, *et al.*, “Nanostructured optical fibers in the SiO₂/SnO₂ system by the sol-gel method,” *Mater. Lett.* **120**, 292–294 (2014).
33. S. Pilz, H. Najafi, M. Ryser, *et al.*, “Granulated silica method for the fiber preform production,” *Fibers* **5**(3), 24 (2017).
34. Figure 1(a) created in Biorender. A. Heidt (2024) <https://BioRender.com/w08s018>.
35. A. D. McLachlan and F. P. Meyer, “Temperature dependence of the extinction coefficient of fused silica for CO₂ laser wavelengths,” *Appl. Opt.* **26**(9), 1728 (1987).
36. S. Unger, A. Schwuchow, J. Dellith, *et al.*, “Optical properties of ytterbium/aluminium doped silica glasses,” *Opt. Mater. Express* **10**(4), 907 (2020).
37. D. Blaser, P. Hänzli, S. Pilz, *et al.*, “Multimode ytterbium-aluminosilicate core optical fibre for amplification and laser applications,” *Fibers* **11**(11), 95 (2023).
38. Coherent, “YSF-HI-HP Product Datasheet,” <https://coherentinc.my.site.com/Coherent/specialty-optical-fibers/PM-YSF-HI-HP>, accessed 2025-01-29.
39. A. Schwuchow, S. Unger, S. Jetschke, *et al.*, “Advanced attenuation and fluorescence measurement methods in the investigation of photodarkening and related properties of ytterbium-doped fibers,” *Appl. Opt.* **53**(7), 1466 (2014).
40. S. Unger, A. Schwuchow, S. Jetschke, *et al.*, “Influence of aluminum-phosphorus codoping on optical properties of ytterbium-doped laser fibers,” *Proc. SPIE* **7212**, 72121B (2009).
41. R. Paschotta, J. Nilsson, A. C. Tropper, *et al.*, “Ytterbium-doped fiber amplifiers,” *IEEE J. Quantum Electron.* **33**(7), 1049–1056 (1997).
42. S. Preble, “Nufern Application Note NuApp-3: UHNA Fiber - Efficient Coupling to Silicon Waveguides,” <https://www.coherent.com/content/dam/coherent/site/en/resources/application-note/components-and-accessories/specialty-optical-fibers/uhna-fiber-efficient-coupling-to-silicon-waveguides.pdf>, accessed 2025-01-29.
43. R. Paschotta, J. Nilsson, A. C. Tropper, *et al.*, “Efficient superfluorescent light sources with broad bandwidth,” *IEEE J. Select. Topics Quantum Electron.* **3**(4), 1097–1099 (1997).
44. L. Di Labio, W. Lüthy, V. Romano, *et al.*, “Superbroadband fluorescence fiber fabricated with granulated oxides,” *Opt. Lett.* **33**(10), 1050–1052 (2008).
45. B. E. Bouma, “Optical coherence tomographic imaging of human tissue at 1.55 μm and 1.81 μm using Er- and Tm-doped fiber sources,” *J. Biomed. Opt.* **3**(1), 76 (1998).
46. Z. Li, A. Heidt, J. Daniel, *et al.*, “Thulium-doped fiber amplifier for optical communications at 2 μm,” *Opt. Express* **21**(8), 9289–9297 (2013).
47. C. Manzoni, O. D. Mücke, G. Cirmi, *et al.*, “Coherent pulse synthesis: towards sub-cycle optical waveforms,” *Laser Photonics Rev.* **9**(2), 129–171 (2015).
48. Y. Kobayashi, E. H. Sekiya, M. Banno, *et al.*, “Effect of P-to-rare earth atomic ratio on energy transfer in Er-Yb-doped optical fiber,” *J. Lightwave Technol.* **38**(16), 4504–4512 (2020).
49. T. Sylvestre, E. Genier, A. N. Ghosh, *et al.*, “Recent advances in supercontinuum generation in specialty optical fibers [invited],” *J. Opt. Soc. Am. B* **38**(12), F90 (2021).
50. G. Agrawal, *Nonlinear Fiber Optics*, 6 Edition (Academic Press, 2019).
51. J. H. Price, X. Feng, A. M. Heidt, *et al.*, “Supercontinuum generation in non-silica fibers,” *Opt. Fiber Technol.* **18**(5), 327–344 (2012).
52. D. Cotter, C. N. Ironside, B. J. Ainslie, *et al.*, “Picosecond pump-probe interferometric measurement of optical nonlinearity in semiconductor-doped fibers,” *Opt. Lett.* **14**(6), 317 (1989).
53. S. Ju, P. R. Watekar, and W.-T. Han, “Fabrication of highly nonlinear germano-silicate glass optical fiber incorporated with PbTe semiconductor quantum dots using atomization doping process and its optical nonlinearity,” *Opt. Express* **19**(3), 2599 (2011).
54. Y. Zhang and Y. Wang, “Nonlinear optical properties of metal nanoparticles: a review,” *RSC Adv.* **7**(71), 45129–45144 (2017).
55. M. Sheik-Bahae, R. J. DeSalvo, A. A. Said, *et al.*, “Optical nonlinearities in diamond,” *Proc. SPIE* **2428**, 605–609 (1995).
56. F. Trojánek, K. Židek, B. Dzurňák, *et al.*, “Nonlinear optical properties of nanocrystalline diamond,” *Opt. Express* **18**(2), 1349 (2010).
57. R. Driben, A. Husakou, and J. Herrmann, “Low-threshold supercontinuum generation in glasses doped with silver nanoparticles,” *Opt. Express* **17**(20), 17989 (2009).
58. S. Bose, A. Sahoo, R. Chattopadhyay, *et al.*, “Implications of a zero-nonlinearity wavelength in photonic crystal fibers doped with silver nanoparticles,” *Phys. Rev. A* **94**(4), 043835 (2016).

59. F. R. Arteaga-Sierra, A. Antikainen, and G. P. Agrawal, "Soliton dynamics in photonic-crystal fibers with frequency-dependent Kerr nonlinearity," *Phys. Rev. A* **98**(1), 013830 (2018).
60. Y. Ruan, H. Ji, B. C. Johnson, *et al.*, "Nanodiamond in tellurite glass Part II: practical nanodiamond-doped fibers," *Opt. Mater. Express* **5**(1), 73 (2015).
61. A. Filipkowski, M. Mrózek, G. Stepniewski, *et al.*, "Volumetric incorporation of NV diamond emitters in nanostructured F2 glass magneto-optical fiber probes," *Carbon* **196**, 10–19 (2022).
62. G. Stepniewski, P. Hänzi, A. Filipkowski, *et al.*, "Nonlinearity shaping in nanostructured glass-diamond hybrid materials for optical fiber preforms," *Carbon* **215**, 118465 (2023).
63. P. Hänzi, D. Pysz, and M. Mrózek, "Laser-assisted rapid prototyping of silica optical fibers functionalized with nanodiamonds and multiple active rare earth dopants [Dataset]," BORIS Portal, 2025, <https://boris-portal.unibe.ch/handle/20.500.12422/205165>.

